Acta Materialia 266 (2024) 119693

Contents lists available at ScienceDirect

Acta Materialia

journal homepage: www.elsevier.com/locate/actamat

Full length article

On-chip very low strain rate rheology of amorphous olivine films

Michaël Coulombier [a,*], Paul Baral [b], Andrey Orekhov [c], Ralf Dohmen [d], Jean Pierre Raskin [e], Thomas Pardoen [a,f], Patrick Cordier [g,h], Hosni Idrissi [a,c]

[a] Institute of Mechanics, Materials and Civil Engineering (IMMC), UCLouvain, B-1348, Louvain-la-Neuve, Belgium
[b] EMSE, UMR CNRS 5307 LGF, Centre SMS, Saint-Etienne, France
[c] EMAT, University of Antwerp, Groenenborgerlaan 171, Antwerp B-2020, Belgium
[d] Institute of Geology, Mineralogy, and Geophysics, Ruhr-University Bochum, Universitätsstr. 150, Bochum 44801, Germany
[e] Institute of Information and Communication Technologies, Electronics and Applied Mathematics (ICTEAM), UCLouvain, B-1348, Louvain-la-Neuve, Belgium
[f] WEL Research Institute, avenue Pasteur, 6, Wavre 1300, Belgique
[g] Univ. Lille, CNRS, INRAE, Centrale Lille, UMR 8207-UMET-Unité Matériaux et Transformations, Lille, France
[h] Institut Universitaire de France, Paris, France

ARTICLE INFO

Keywords:
Rheology
Amorphous olivine
Nanomechanical testing
Relaxation
Thin film

ABSTRACT

Recent observations made by the authors revealed the activation of stress induced amorphization and sliding at grain boundary in olivine [1], a mechanism which is expected to play a pivotal role in the viscosity drop at the lithosphere-asthenosphere boundary and the brittle-ductile transition in the lithospheric mantle. However, there is a lack of information in the literature regarding the intrinsic mechanical properties and the elementary deformation mechanisms of this material, especially at time scales relevant for geodynamics. In the present work, amorphous olivine films were obtained by pulsed laser deposition (PLD). The mechanical response including the rate dependent behavior are investigated using a tension-on-chip (TOC) method developed at UCLouvain allowing to perform creep/relaxation tests on thin films at extremely low strain rates. In the present work, strain rate down to 10^{-12} s^{-1} was reached which is unique. High strain rate sensitivity of 0.054 is observed together with the activation of relaxation at the very early stage of deformation. Furthermore, digital image correlation (DIC), used for the first time on films deformed by TOC, reveals local strain heterogeneities. The relationship between such heterogeneities, the high strain rate sensitivity and the effect of the electron beam in the scanning electron microscope is discussed and compared to the literature.

1. Introduction

Olivine is a family of minerals with an orthorhombic structure and a general composition of (Mg, Fe)$_2SiO_4$. The Mg_2SiO_4 magnesium-rich end-member is called forsterite, and the Fe_2SiO_4 iron-rich end-member is called fayalite. With an iron composition close to 10 %, olivine is the main constituent of the Earth's mantle down to a depth of 410 km. A deeper appraisal of the mechanical properties of olivine is therefore of major interest for understanding and modeling mantle dynamics and plate tectonics. It has recently been shown that olivine grain boundaries can amorphize and slide under high stress in olivine [1]. Stress-induced intragranular amorphization has also been reported by [2]. Approaching the glass transition temperature, the grain boundary amorphization and sliding mechanism can have a significant impact on the olivine rheology. Samae et al. 2021 [1] have suggested that it may be a mechanism behind the abrupt change of the rheological properties at the lithosphere-asthenosphere boundary. Below this temperature, the presence of this amorphous intergranular film may impact the brittle-ductile transition in the lithospheric mantle. Understanding the mechanical properties of amorphous olivine (a-olivine) has therefore become a subject of great interest [3]. But this material is not easy to generate. It has hardly been observed except in shock [4] or diamond anvil cell experiments [5]. Indeed, olivine glass is extremely difficult to preserve by quenching from the melt [6]. Pulsed laser ablation is a technique that enables amorphous films to be deposited at quench rates high enough to preserve a-olivine [7]. Studying these films, however, requires the use of appropriate techniques, especially in the context of exploring mechanical properties. Baral et al. [8] used nanoindentation to carry out the first mechanical characterization of a-olivine. In particular, the strain-rate sensitivity of a-olivine was characterized

* Corresponding author.
E-mail address: michael.coulombier@uclouvain.be (M. Coulombier).

https://doi.org/10.1016/j.actamat.2024.119693
Received 24 July 2023; Received in revised form 23 November 2023; Accepted 16 January 2024
Available online 17 January 2024

down to ca. $10^{-7}s^{-1}$ using relaxation tests. In the field of Earth sciences, the difference between experimental strain-rates and those operating in nature is a major difficulty. We show in this work that the TOC technique, which is well-suited to study thin-film materials, can be used to push the current limits in this field. The present study is conducted on the same material as the one used in [8].

2. Material and methods

2.1. Pulsed laser deposited a-olivine

Synthetic, polycrystalline pellets of olivine with a nominal composition of $Fe_{0.2}Mg_{1.8}SiO_4$ were ablated using a pulsed laser beam with a frequency of 10 Hz, a wavelength of 192 nm, and at a laser fluence of approximately 5 J/cm^2. Details on the setup can be found in [7]. The pellets were grinded before deposition to minimize grooving during deposition and to maintain parallelism between pellets and sample. The deposition rates were in the 10–20 nm/min range and were performed under background vacuum pressure of 1×10^{-5} mbar (1×10^{-3} Pa) at room temperature. These conditions ensure that the silicate film has an olivine-like composition and is amorphous and chemically homogeneous [7,9].

2.2. TEM characterization

The initial microstructure of PLD a-olivine was investigated on classical Focused Ion Beam (FIB) cross-sectional a-olivine thin foils lying on the silicon substrate. In this case, a Pt protection layer was deposited in two steps – by electron beam, then by ion beam– in order to avoid FIB damage at the sample surface. The FIB foils were thinned to a thickness < 50 nm. An ion beam of 2 kV/0.2 nA was employed for final thinning of the specimen and to minimize irradiation damage generated during high-voltage FIB thinning. TEM characterizations were conducted in a FEI Osiris microscope equipped with highly efficient SuperX Energy Dispersive X-ray (EDX) system operated at 200 kV. Z-contrast images were recorded in scanning transmission electron microscope (STEM) mode with convergence angle of 115–157 mrad using HAADF-STEM detector.

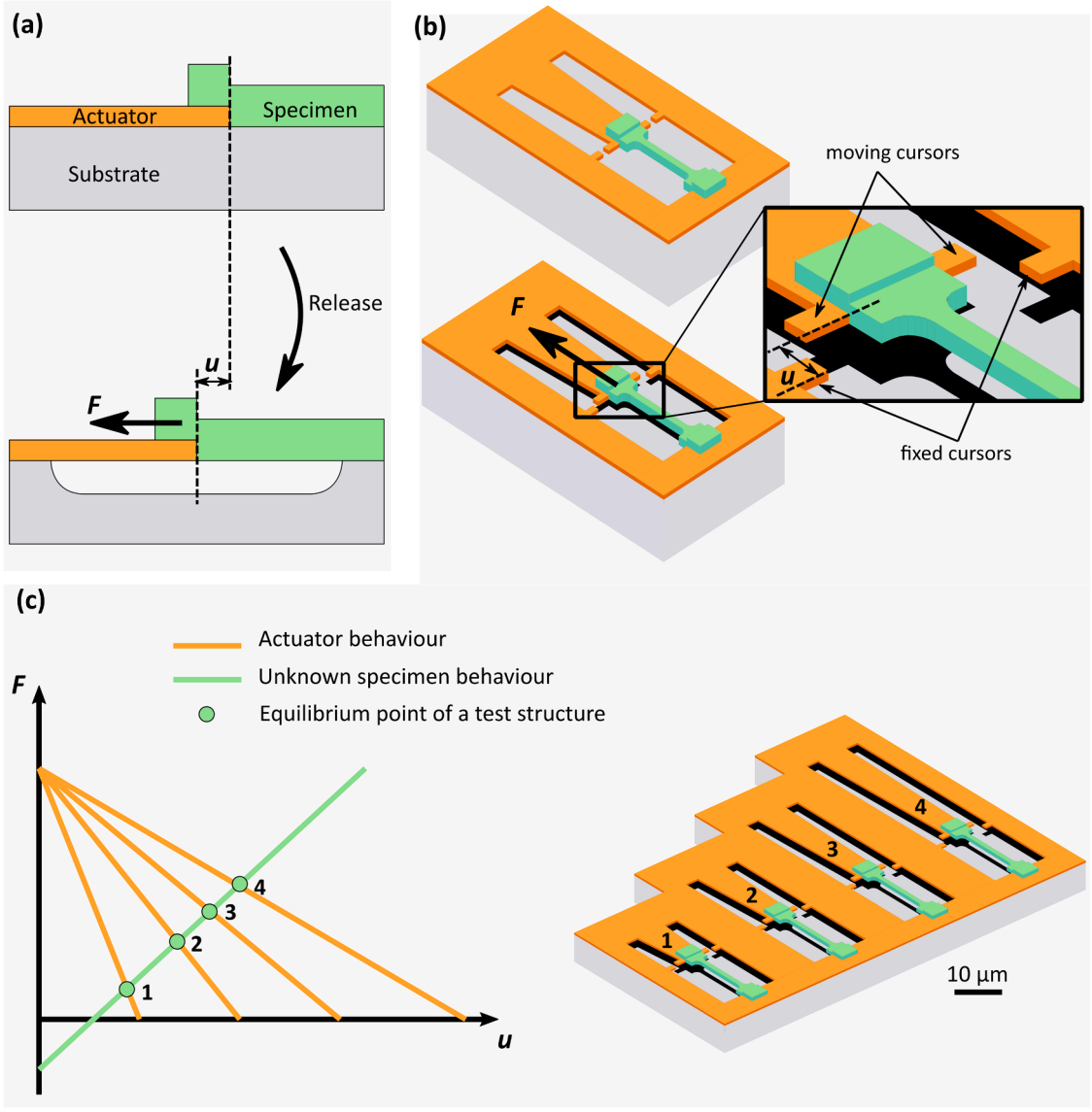

Fig. 1. (a) and (b) Release of an elementary tensile test structure of TOC. The resulting displacement u is highlighted in the inset. (c) Force – displacement diagram for a series of actuators with different lengths pulling on identical specimen beams. The equilibrium point reached after release is highlighted and the corresponding arrangement of a suite of elementary tensile test structures is shown.

2.3. Tension-on-chip

Uniaxial tensile tests have been performed using a tension-on-chip (TOC) technique [10] which relies on residual stresses generated in an "actuator layer" to pull on a "specimen layer". Fabrication involves deposition, etching and lithography to generate the configuration shown in Fig. 1a and b. The actuation is performed by etching the substrate located underneath the actuator and specimen beams. This etching is performed in gas phase using XeF_2 as in [11] and releases the residual stresses which lead to uniaxial tension on the freestanding specimen.

An equilibrium position is reached and the generated displacement u can be measured by scanning electron microscopy (SEM) through cursors (see insert of 3D view in Fig. 1b). The displacement between the fixed cursor and moving cursor enables the extraction of the engineering strain in the deformed specimen using

$$\varepsilon = \frac{u}{L_0} - \varepsilon_{mis} \tag{1}$$

where u is the distance between fixed and moving cursors, L_0 is the initial length of the specimen beam and ε_{mis} is the mismatch strain of the specimen layer.

The actuator has a known behavior and acts as a linear spring. Hence, it can be used as a force sensor. The equilibrium position reached after etching the substrate enables to extract the force applied to the specimen which can be converted into the applied stress by measuring cross sections of both actuator and specimen beams. The engineering stress in the deformed specimen is thus given by

$$\sigma = E_a \frac{w_s t_s}{w_a t_a} \left(\frac{u}{L_{0a}} - \varepsilon_{mis\ a} \right) \tag{2}$$

A single test structure provides thus a couple displacement – force (u, F) which can be converted into a couple engineering strain-engineering stress (ε, σ) by Eqs. (1) and (2) provided that the Young's modulus (E_a), length (L_{0a}), width (w_a), thickness (t_a) and mismatch strain of actuator material ($\varepsilon_{mis\ a}$) are known together with length (L_0), width (w), thickness (t) and mismatch strain of specimen material (ε_{mis}).

The SEM used for the measurements of the specimen and actuator beam dimensions is an AURIGA Zeiss. The displacement u is the mean value of the displacements measured on both sides of the actuator beam at the highest possible magnification still allowing the two cursors to be observed in the same image (x10,000). This enables possible misalignment between SEM pictures and tensile axis to be taken into account.

Photolithography allows the design of many test structures at the same time; the same geometry of specimens is multiplied while actuator length is varied to access a wide range of strains. This configuration is illustrated in Fig. 1c. In a force-displacement graph, the varying actuator length translates into a span of lines with identical origin point but with different slopes (different spring constants). The equilibrium point of each test structure is different which gives access to different levels of displacement-force. In the practice, test structures are grouped in series of identical specimen geometry. The specimen geometry is varied from one series to another to extract the entire uniaxial tension mechanical response of the specimen material. The longer the specimen the smaller the applied strain and conversely.

2.4. Methodology for the extraction of the strain rate sensitivity

The use of TOC to extract the strain rate sensitivity has been reported previously for metallic thin films in [12]. It is adapted here to a-olivine thin films.

A prior condition to study relaxation of the specimen material is that the actuator material does not show any time dependent response. This has been validated for the LPCVD Si_3N_4 used in this study as in [12].

After reaching a stable position at time t_0, relaxation can take place in the deformed specimen. During relaxation, the strain in the specimen will increase while the stress will decrease following the linear F- u relationship imposed by the actuator beam (see Fig. 2a). This situation corresponds to a relaxation test performed on a specimen attached to a spring. The displacement is thus measured n times in the SEM (Fig. 2b) and the sample is stored under N_2 atmosphere between measurements in order to avoid any alteration.

The early stages of relaxation (from t_0 to t_1) cannot be recorded as the displacement measurement is not performed in situ while etching the silicon substrate. The first displacement measurement is thus performed at time t_1, about an hour after actuation. The engineering stress-engineering strain data are computed from the measurements on all test structures performed at time t_1. For each test structure, the n next displacement measurements provide a discrete variation of displacement and force with time. It must be noted that the time interval between measurements is selected so as to ensure a variation of displacement ($u(t_n)$ - $u(t_{n-1})$) large enough to be detected.

The rate sensitivity exponent defined as $m = d\ln\sigma / d\ln\dot{\varepsilon}$ can be extracted for each test structure undergoing stress relaxation using the methodology summarized in Fig. S1. The engineering strain and stress are computed from the displacement-time data using Eqs. (1) and (2) respectively. The stress is converted to plastic strain by subtracting the elastic contribution $\varepsilon_{el} = \sigma/E$, E being the Young's modulus of the specimen material extracted from the stress-strain data from all TOC test structures. The plastic strain rate can also be computed as $\dot{\varepsilon}_p = (\varepsilon_{p2} - \varepsilon_{p1})/(t_2 - t_1)$. As a result, each time a measurement is performed, the stress and plastic strain rate are known. Each relaxing test structure thus provides a series of stress-strain rate couples which are then reported in a log-log plot, showing a linear trend. By definition, the slope of that line is the strain rate sensitivity parameter. The method could thus provide precious information on the rate dependent behavior of thin films.

2.5. Unloading of single tensile test structure

The residual stress driven actuator used in TOC cannot be controlled such as a piezoelectric actuator or such as the tip of a nanoindentor which prevents the unloading of deformed specimens.

However, a FIB instrument can be used as a cutting tool to alter the equilibrium position of the system actuator-specimen. The methodology is illustrated in Fig. 3. The gallium ion beam is used to cut the actuator part of a single tensile test structure. The cut is performed a few tenth of microns from the overlap between the actuator and the specimen with a low probe current (30 kV, 50 pA) in order to avoid any charging effect which could alter the planarity of the specimen beam. After cutting, the force on the specimen is zero and the specimen is shorter by an amount u_{unload}. This new equilibrium position can be measured through the resulting displacement between movable and fixed cursors ($u - u_{unload}$). This operation can be performed at any time during the relaxation process of a test structure but it is irreversible.

Just before FIB cutting the strain and stress are respectively $\varepsilon(t_n)$ and $\sigma(t_n)$ (see Fig. 3a). Once unloaded, the force applied to the specimen is zero and so is the stress. The strain can be determined as $\varepsilon = \frac{u(t_n) - u_{unload}}{L_0} - \varepsilon_{mis}$.

These two points give access to a measurement of the Young's modulus of a-olivine. It can also be used to determine the overall contribution of the elastic strain to the total strain.

2.6. Digital image correlation

In Section 2.3, the extraction of the overall mechanical behavior of the specimen material (engineering stress-strain curve) relies on the displacement of cursors as a measurement tool. Digital Image correlation (DIC) takes this a step further by examining the local strain field at the surface of the deformed specimen. The methodology is similar to the one recently developed by Klavzer et al. [13] for compression of fiber-reinforced composites. In this case, an indium physical vapor

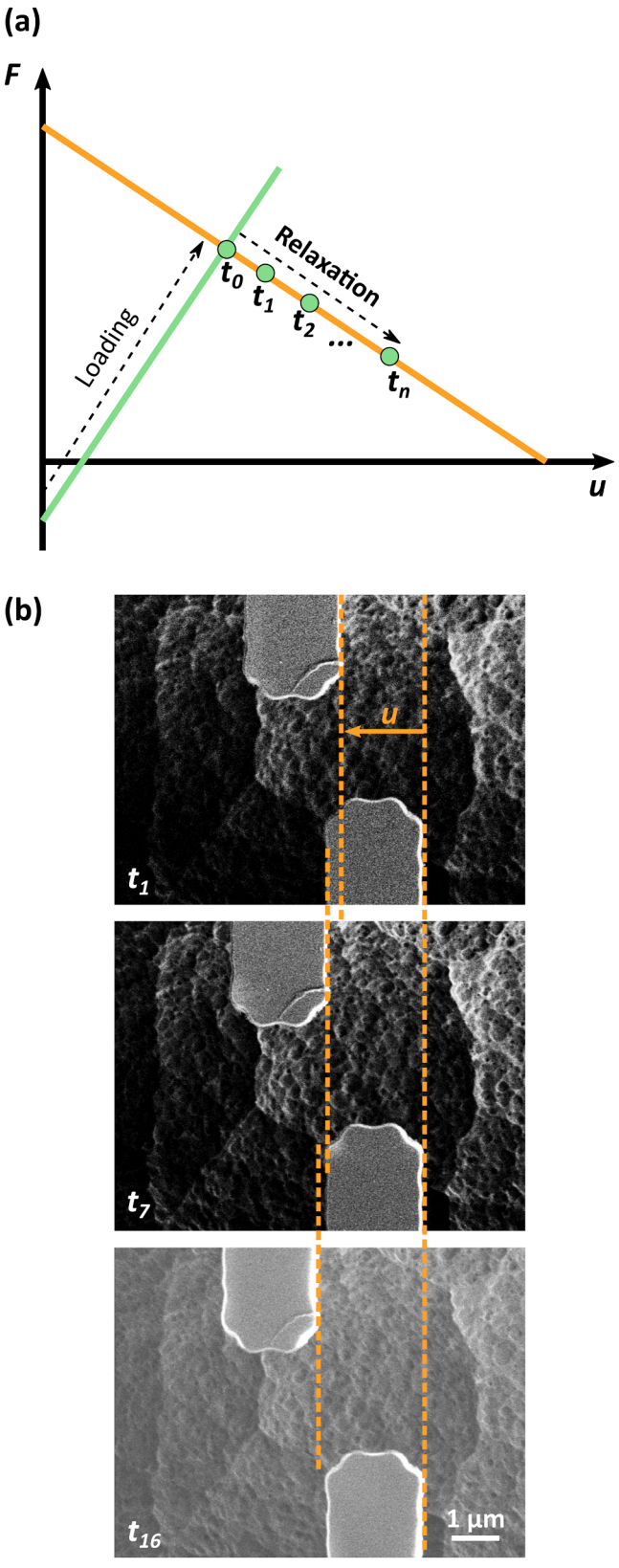

Fig. 2. (a) Force – displacement diagram for the actuator and the specimen beam of one elementary tensile test structure with equilibrium point attained during the release (t_0) and subsequent relaxation points (t_1 to t_n), (b) displacement measurement based on cursors for a representative test structure at time t_1 = 30 min, t_7= 8 days and t_{16} = 2 years.

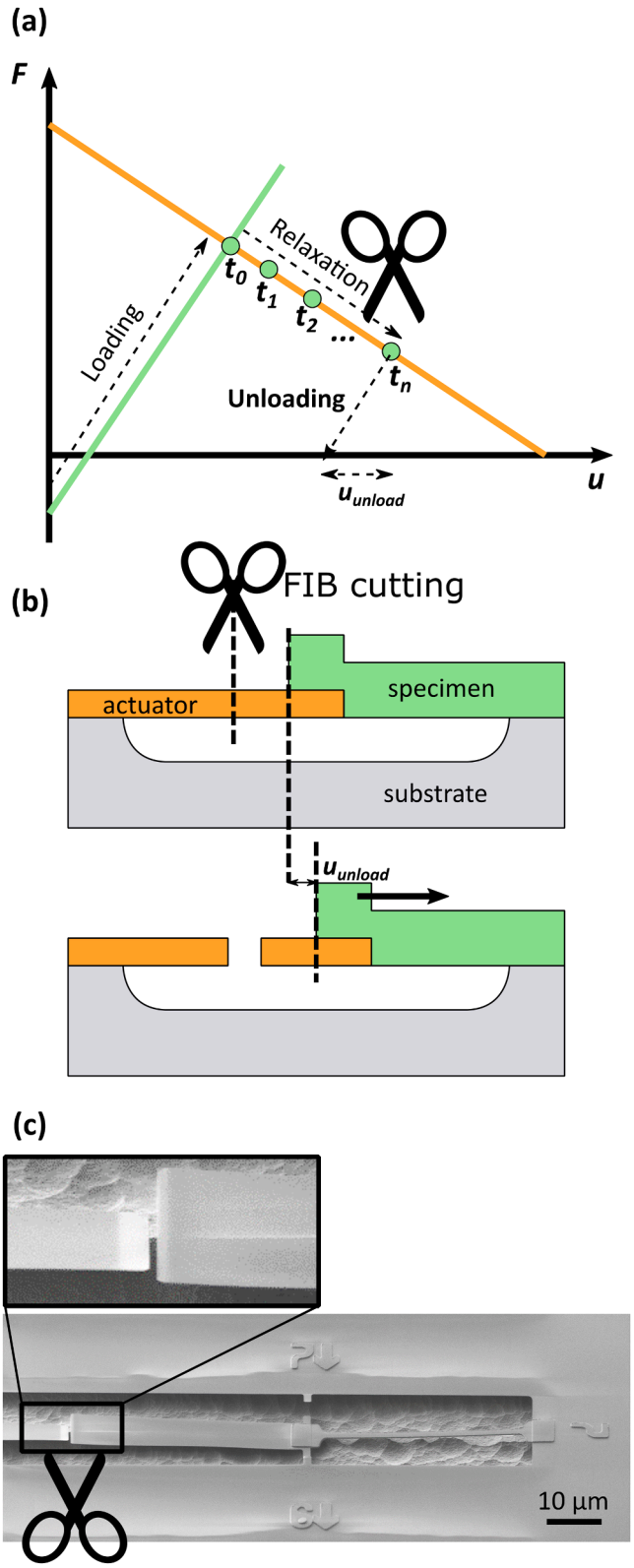

Fig. 3. Methodology for unloading of test structures. After a specific relaxation time, the FIB is used to cut the actuator which releases the residual stresses in the specimen. The cutting is illustrated in (a) a force-displacement diagram, (b) schematic side view of the elementary tensile test structure, (c) SEM picture of a 50 µm-long specimen.

deposition is used to generate a nanometric DIC speckle.

2.6.1. Speckle pattern

The indium electron beam evaporation is performed right after deposition of a- olivine and before lift-off so that the speckle is deposited only on the specimen material (Fig. 4). Indium pellets with 99.99 % purity are used. The deposition rate was kept equal to 1 Å.s^{-1} and the deposition time was set to reach 5 nm thickness. This low thickness leads to a non-continuous film with heterogeneous particles. The particles adhere to the material surface and do not affect the mechanical response nor the deformation behavior since they are not connected to each other. The particles' radius follows a normal distribution with 8.1 nm average value and standard deviation equal to 2.8 nm. This distribution is identical to the one tested by Klavzer et al. [13] for a 5 nm-thick indium film. As already discussed by Klavzer et al. [13], this deposition condition is optimal for the chosen field of view. Indeed, for higher film thickness, the particles are too small to be observed for the chosen field of view.

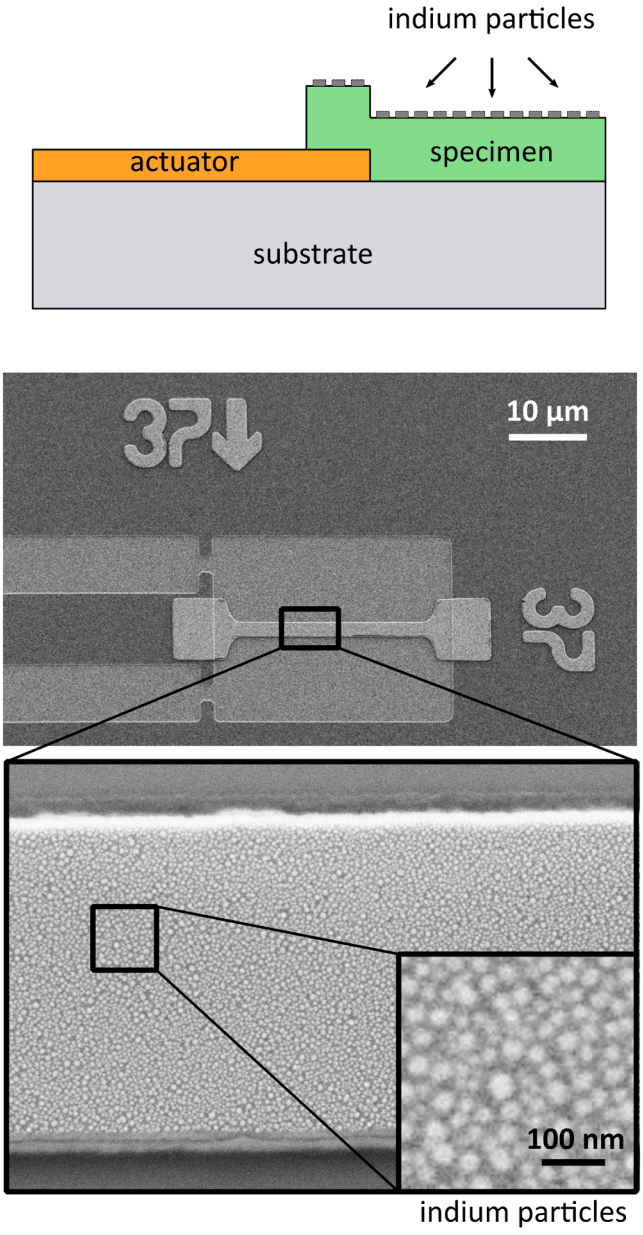

Fig. 4. Speckle pattern for DIC measurements 5 nm-thick indium speckles deposited by e-beam evaporation on an a-olivine specimen prior to release.

2.6.2. SEM observations

The sample used for DIC analysis was similar to the one used for the extraction of the stress-strain curve but the focus was made on short specimens (25 µm long) to catch the higher strain regime. The analysis is different than with standard DIC where the speckle can be followed at different stages of the deformation process. Here, a scan is performed on specimens prior to release and another scan is performed after reaching the equilibrium position. Therefore, it is not an in situ measurement *per se* and only the initial and the deformed position can be measured.

The sample was mounted on a stub and maintained with silver paste to ensure good electrical contact and to limit charging effects during observation. All observations were performed after a settling time of minimum 10 min after sample mounting in the SEM chamber so that mechanical drift stabilizes to low values. Images were taken with a Zeiss AURIGA SEM equipped with a secondary electron detector. All images were obtained at a magnification of x30k, electron high voltage of 2 kV and working distance of 6.8 mm. Five frames scans were averaged with a relatively high scan speed in order to avoid long duration single frame where drift may significantly distort the image. In order to perform image analysis, one image per specimen was taken before the release of the test structures. After the release, images were taken at the same locations at different time intervals to observe any evolution in the strain field under relaxation.

2.6.3. DIC analysis

Strain maps are obtained using the Matlab script Ncorr developped by Blaber et al. [14]. The subset size is set to 15 pixels radius and the subset spacing is set to 1 pixel. The subset size refers to a group of pixels in which strains are assumed to be homogeneous, while the subset spacing denotes the spatial shift between two adjacent subsets. The later defines the spatial resolution of the DIC measurements. The three components of the strain tensor are computed using the Lagrangian strain theory by fitting the displacement field over 8×8 pixels square, which corresponds to a strain radius of 4 pixels. This third fitting parameter is set to ensure a minimum of 1 pixel displacement gradient within the subset, which limits the numerical derivative noise. Increasing the size of the fitted displacement field leads to smoothed strain field and lower spatial resolution of the strain heterogeneity. These parameters have been found to be representative of the spatial heterogeneities without introducing too much numerical noise. In this study, the chosen parameters lead to a spatial resolution between 50 and 100 nm, which means that smaller spatial heterogeneities cannot be captured. A parametric study is presented in supplementary (See Fig. S2) to highlight the evolution of the strain field as a function of subset radius and strain radius. It is worth noting that for all the sets of parameters, the strain field exhibits the same heterogeneous character.

3. Results

3.1. PLD amorphous olivine characterization

Fig. 5a shows bright-field (BF-TEM) image obtained on cross-sectional thin foil prepare by FIB on as-deposited a-olivine film with thickness of 280 nm while Fig. 5b exhibits high resolution TEM (HRTEM) image on the same film. In this figure, both the image and the Fast Fourier Transform (FFT in the top right inset) confirm that the initial microstructure of the olivine film is fully amorphous. This is in agreement with the selected area diffraction pattern (SADP) shown in Fig. 5a which reveals the presence of two diffuse rings. Fig. 5c exhibits HAADF-STEM image and the corresponding STEM-EDX maps of Si, O, Mg, Fe and Pt. An intensity line profile of the Kα of the main atomic constituent of a-olivine is shown in Fig. S4 and shows local variation of the composition at a scale of about 25 nm. In addition, the HAADF-STEM image shows the presence of a black line close to the substrate (white

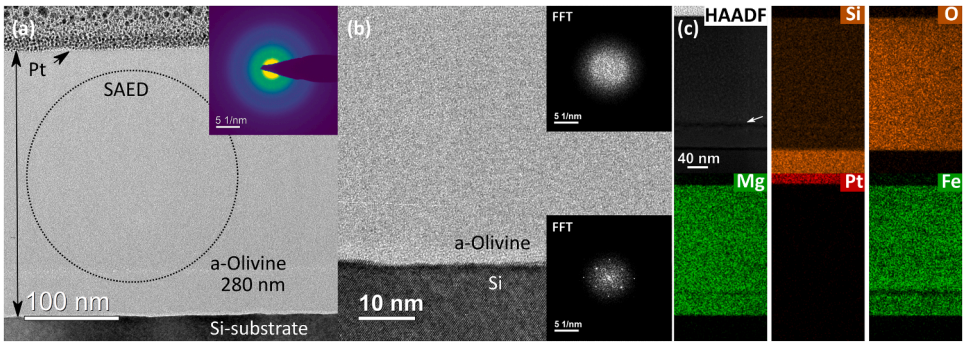

Fig. 5. (a) Bright-field TEM image of a cross-sectional view of a-olivine film on Si substrate. (b) High resolution TEM with corresponding FFTs from the film and substrate. (c) EDX maps show the distribution of elements across the a-olivine film.

arrow in Fig. 5c). This defect which can also be observed in some EDX maps is probably due a technical problem that occurred during pulsed laser deposition.

3.2. Engineering stress-strain data from TOC

All the TOC test structures considered in this paper come from the same silicon die. Hence, the fabrication steps are the same for all the test structures while the geometry of specimens is different. Six series of test structures are considered. The geometry of specimen beams is the same within the series and is sketched next to the engineering stress strain data of Fig. 6a,b along with their designed widths and lengths. Most test structures have a dog-bone shape with the specimen being wider at extremities (Fig. 6a) while the longest ones, corresponding to small strain (Fig. 6b), have a perfectly rectangular shape.

While the thickness of Si_3N_4 measured by ellipsometry is identical for all actuators, the thickness of specimen beams shows a thickness gradient at the die level which is inherent to the deposition setup [7]. This is taken into account for the stress calculation as the thickness was measured prior to actuation by profilometry for all specimens with values lying between 160 nm and 300 nm.

The Young's modulus of silicon nitride is taken as 250 GPa as extracted from earlier work on the same LPCVD Si_3N_4 [15]. The mismatch strain of silicon nitride required to extract the engineering stress in the specimen is measured on dedicated test structures (free-standing cantilevers similar to the ones used in [16]. The extracted value is $\varepsilon_{mis\ act} = -0.0325$.

A-olivine shows compressive stresses upon deposition. The corresponding mismatch strain could not be extracted from cantilever beams due to the presence of a small stress gradient over the thickness that caused out-of-plane bending of the beams. Instead, the mismatch strain of a-olivine is determined by assuming that the extrapolation of small stress-strain data meets the axis at (0,0). The extracted value is equal to 0.00105.

The engineering stress-strain data obtained using Eqs. (1) and (2) with displacements measured one hour after actuation are shown in Fig. 6a. The small stress-strain data corresponding to wider and longer specimens are highlighted in Fig. 7b.

Only the data from test structures where the displacement is significantly high enough to get trustful stress and strain values are considered in Fig. 6. The error bars in this figure reflect the uncertainty on the stress and strain considering an error of 20 nm on the displacement measurement while no error is considered on the other parameters.

In all cases, 800 μm and 400 μm long test structures were deformed without occurrence of fracture. The case of the 100 μm long test structures is particular as local lithography problems prevented full release of the actuator beams. As a consequence, only one 100 μm-long test structure is shown if Fig. 6a. The 50 μm-long test structures were all deformed but the specimen beams experiencing the larger strains were broken at the overlap between the specimen beams and actuators. Finally, the 25 μm-long specimens were all deformed without occurrence of fracture.

Eq. (1) used to extract the engineering strain in the specimen considers an infinite stiffness for the two wider parts of the dog-bone specimens. Actually, the wider parts deform elastically and the overall displacement u is the sum of two contributions u_{gauge} and u_{db}, the elongation of the specimen gage length and wider parts, respectively. The contribution of u_{db} becomes more important as the specimen length decreases. In order to avoid inaccuracies associated to the deformation of the wider parts, the Young's modulus is extracted from a linear fit on the stress-strain data of the longest specimens (800 μm) which have a perfect rectangular shape. The extracted Young's modulus is equal to 107 GPa and this value is then used to account for the finite stiffness of the wider part for specimens with length of 25, 50, 100 and 400 μm. The engineering strains represented in Fig. 6a are the corrected values considering the elasticity of the wider parts of the specimen.

While the first displacement measurement on each test structure enables the determination of the stress-strain data of Fig. 6a,b, the monitoring of the displacement with time delivers the subsequent stress relaxation. Stress relaxation has been observed on all test structures and has been measured over a 2 years span time, which is unique. The amplitude of the stress relaxation after 2 years is shown in Fig. 6a and b for the most deformed test structure of each series. All in-between measurements lie in the line connecting first and final measurement (the dashed arrows of Fig. 6a and b). This linear trend originates from the spring-like behavior of actuators.

After 5 months of stress relaxation, 4 test structures from 4 different series have been unloaded using the technique described in Section 2.4. For these four test structures, the out of plane deflection resulting from FIB cutting generates an error in the displacement measurement approximately equal to one pixel and can thus be neglected. The resulting position in the engineering stress – engineering strain graph is displayed in Fig 6c and d along with the extracted Young's modulus.

3.3. Extraction of the strain rate sensitivity

All a-olivine specimens shown in Fig 6a and b experience stress relaxation which can be measured from the monitoring of the displacement between the fixed cursor and moving cursor. At some point, the displacement evolution between two measurements becomes so small that only the most deformed specimens from each series were followed i.e. the ones with the longest actuators. As a result, the methodology for strain rate sensitivity extraction has been applied to the relaxation data coming from 13 test structures from 3 different sets of specimen length (100, 400 and 800 μm). The stress – plastic strain rate data are reported in Fig. 7 and the mean value of the strain rate sensitivity of identical specimen geometry is highlighted (0.033, 0.049 and 0.055 for 100, 400 and 800 μm, respectively). The most relevant

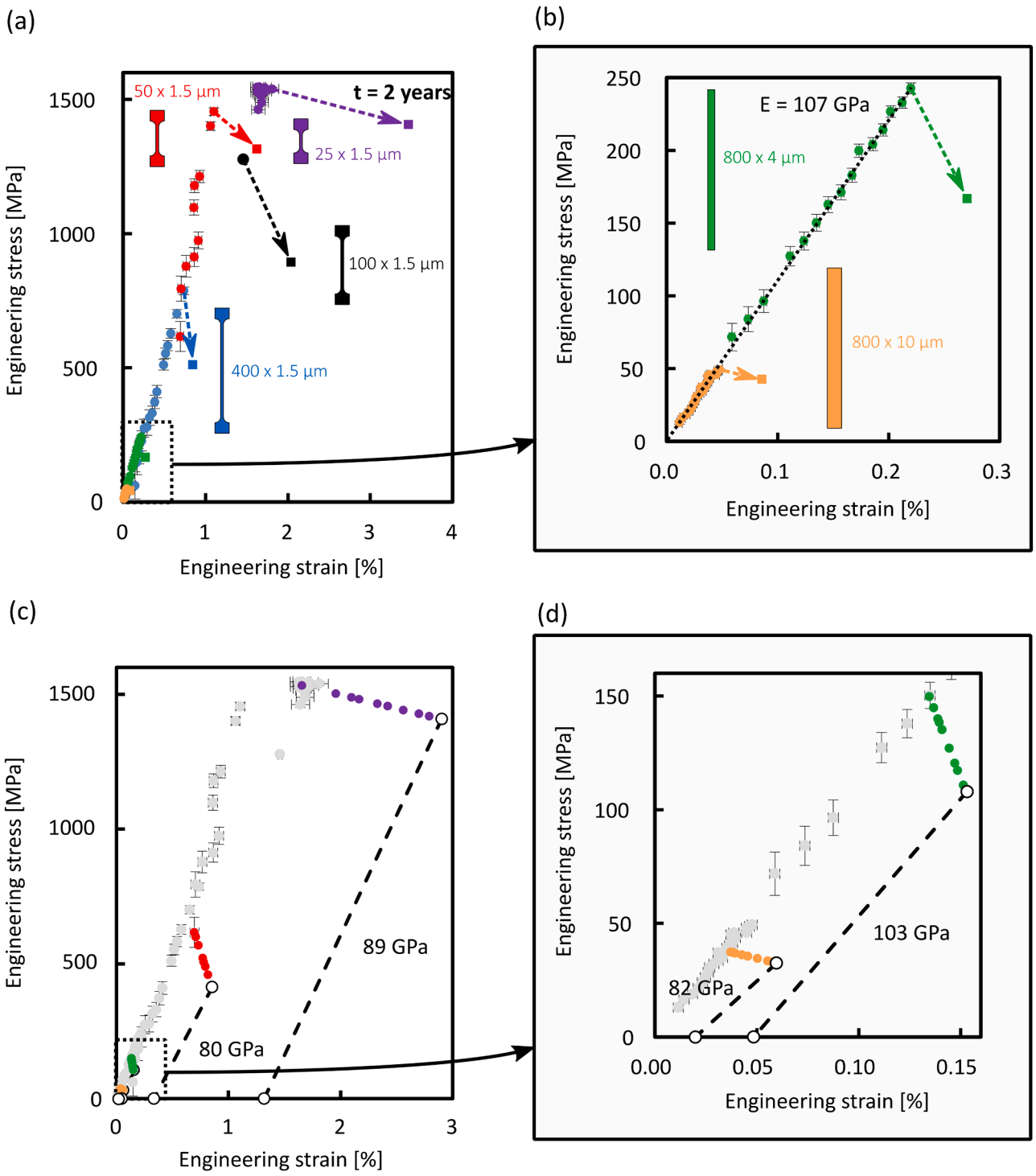

Fig. 6. (a) and (b) Engineering stress strain curve extracted from TOC of an a-olivine thin film. The relaxation after 2 years is shown for the last test structure of each specimen geometry. (c) and (d) Unloading of relaxed test structures for 4 specimens with corresponding extracted Young's modulus.

parameters of these 13 test structures are reported in Table 1. It includes the maximum evolution of elongation between the first measurement (t_1 = 1 h) and the last measurement (t_{16} = 2 years), the initial strain as measured at time t_1, the corresponding initial stress and the strain rate sensitivity.

Even if the 25-µm long specimens were not considered here due to the difficulty to take the relaxation of the wider parts of the specimens into account, the case of the most deformed test structure (B11 1.5 25 50) is worth mentioning. Being the most deformed test structure on the whole silicon die, this specimen was observed in details during the first SEM session. Relaxation data indicate that the specimen underwent faster relaxation with respect to specimens with similar geometry and similar initial strain which is attributed to an electron beam effect. As a result, special care was taken to not directly irradiate specimens with the electron beam. All the displacement measurements were performed on the cursors (see Fig. 2) and not on the specimen layer. Consequently, it can be stated that all the relaxation data from Table 1 are not affected by the electron beam.

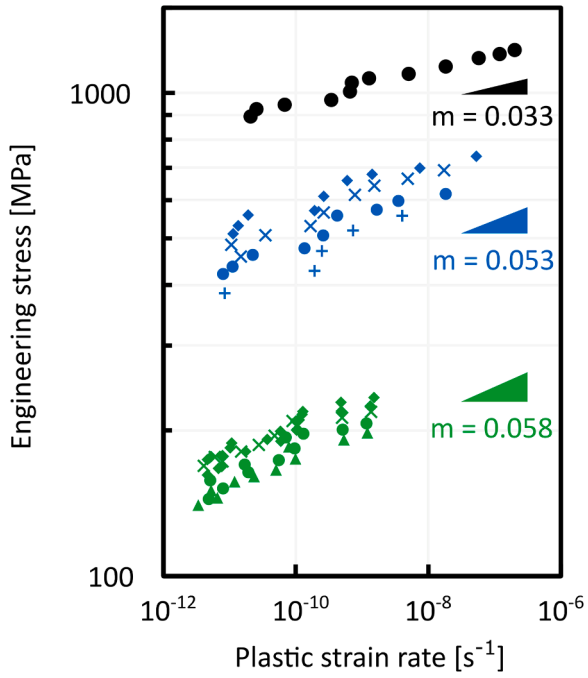

Fig. 7. Engineering stress as a function of plastic strain rate during relaxation for 10 different tensile test specimens. Each symbol relates to one specific test structure. The average strain-rate sensitivity or slope of the data in the log-log graph is displayed for each of group of test structures (undergoing similar range of initial plastic strain).

Table 1
Mechanical data extracted from the 13 relaxation tests of freestanding a-olivine. Δu max is the change of elongation that occurred in the specimen in the 2 years relaxation. ε_{init} and σ_{init} are initial engineering strain and stress measured just after release respectively. m is the strain rate sensitivity parameter extracted after the 2 years relaxation.

Sample	Δu max [nm]	ε_{init} [%]	σ_{init} [MPa]	m [-]
B11 4 800 16	290	0.19	204	0.0584
B11 4 800 17	325	0.20	213	0.0631
B11 4 800 18	336	0.20	226	0.0565
B11 4 800 19	360	0.21	232	0.0570
B11 4 800 20	400	0.22	242	0.0569
B11 1,5 400 24	215	0.55	583	0.0624
B11 1,5 400 25	244	0.58	633	0.0513
B11 1,5 400 27	319	0.66	705	0.0561
B11 1,5 400 29	389	0.75	779	0.0431
B11 1,5 100 25	535	1.49	1260	0.0331

3.4. Digital image correlation

Five test structures similar to the one shown in Fig. 4 have been systematically characterized to extract the displacements and corresponding strain maps as a function of relaxation time. The evolution of the strain distribution is illustrated in Fig. 8 for a test structure having the following dimensions 1.5 μm wide, 25 μm long and 210 nm thick. SEM images have been acquired in the center of the specimen at 30k magnification which covering a window of around 3 μm x 4 μm.

Fig. 8 shows the Lagrangian strain ε_{xx} (x being the horizontal loading direction) as a function of relaxation time. The local strain varies locally from 0 to 7 % while the specimen is submitted to an engineering strain equal to 1.6 %. These local strain values are indicative since the spatial resolution plays a role in their calculation as shown in the supplementary (see Fig. S2). The global strain, on the region of interest, calculated from DIC with the first observation (after 1 h relaxation) is consistent with the macroscopic strain determined from the cursors displacement.

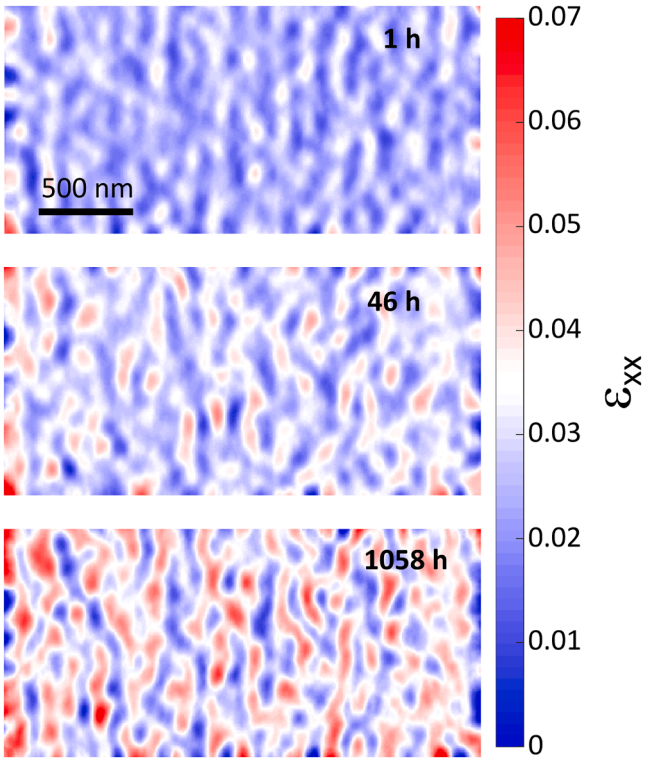

Fig. 8. Lagrangian strain ε_{xx} in the middle of a deformed a-olivine specimen at 3 different relaxation time (x being the horizontal loading direction) as extracted from DIC. The engineering stress calculated from the displacement between cursors is respectively 1191 MPa (1 h), 1036 MPa (46 h) and 900 MPa (1058 h).

For the specimen shown in Fig. 8, the first measured strain from displacement cursors is equal to 0.0175 with a corresponding stress equal to 1191 MPa. The averaged longitudinal strain ε_{xx} on a 3 μm^2 surface from DIC is equal to 0.022. For all five test structures considered in this paper, the global strain extracted from DIC is larger than the one calculated from displacement measurement. This difference could be attributed to an accelerated relaxation associated by the beam effect but the fact that both strain measurements have similar evolution as relaxation proceeds proves experimentally that the Ncorr methodology is robust.

Moreover, Fig. 8 shows that the spatial distribution of highly deformed regions does not vary during deformation, just increasing in amplitude. Further deformation proceeds preferentially at already deformed locations. Plastic deformation spreads from high strain nuclei. This can be observed in more detail on Fig. 9a where isovalue of strain are plotted as a function of relaxation time. Deformed regions overlap and spatially spread, as relaxation increases. The evolution of the strain field with time is also illustrated in Fig. 9b where strain levels in tensile axis show a Gaussian distribution where the mean value increases with relaxation time while the distribution flattens.

In a previous campaign performed to test the DIC methodology, pictures were acquired several times at different magnifications to identify the best conditions for further analysis. DIC analysis revealed the presence of plastic localization at the left of the scanned zone. In SEM, the left side of the scanned zone undergoes longer beam exposure as a pause in the beam movement is usually applied before scanning a new line, a feature known as flyback delay [17]. This was an alert regarding possible influence of a beam effect. As a result, DIC on the five specimens was performed on a single scanned region to reduce the beam time exposure.

DIC giving access to the strain map in two dimensions, the Poisson ratio of a-olivine is quantitatively calculated based on the average

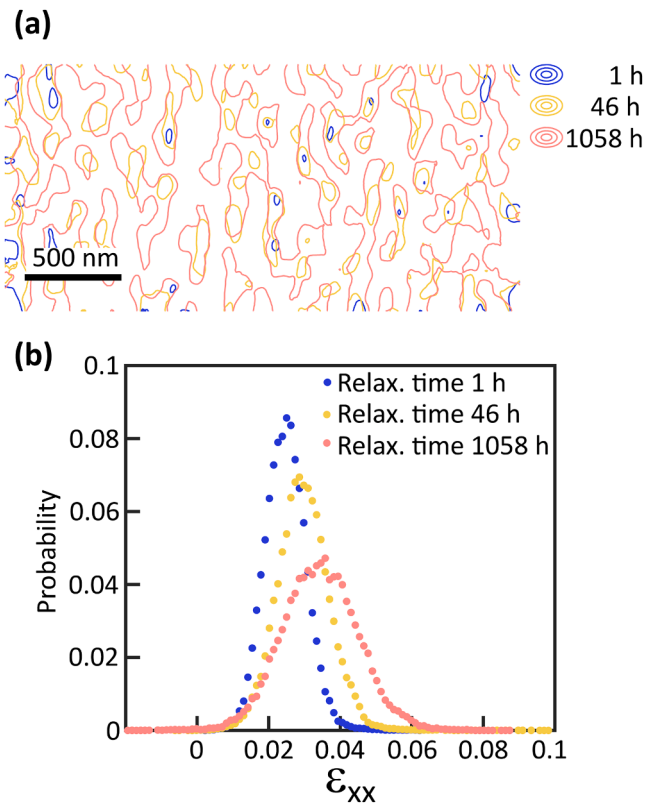

Fig. 9. (a) Iso-value of strain in the middle of a deformed a-olivine specimen as a function of relaxation time. (b) Evolution of strain field with time extracted from DIC.

strains, ε_{xx} and ε_{yy}, evaluated within a 1290 x 617 nm^2 region of interest. One hour after the release, the Poisson ratio calculated for 5 specimens deformed between 0.0161 and 0.0209 strain is equal to 0.29±0.03. This value tends to increase within the studied range of relaxation time (and potentially electron irradiation time). After 44 days, the Poisson ratio is equal to 0.37±0.04.

4. Discussion

4.1. Plastic behavior of a-olivine

The engineering stress-strain response of a-olivine of Fig. 6a shows a linear behavior up to ~1.4 GPa. Only the smallest specimens (25 μm) deviate from the linear trend while the behavior upon further loading cannot be extracted. Indeed, the design of test structures for 25 μm long specimens is such that the maximum pulling force is applied. As a consequence, the maximum engineering strain generated for free-standing a-olivine upon loading was 1.8 % and fracture was not observed. 50 μm long specimens fractured upon loading but cracking occurred at the overlap between actuator and specimen beam. This happened in this series of specimens because the stress concentration at the overlap was larger than the one in the gage length of the specimen. This has to do with the conformity of the deposition technique and with the thickness ratio between actuator and specimen layer. Conformity is hardly controllable as it is inherent to the parameters used on the PLD setup to deposit amorphous olivine. Some shadowing effect due to deposition on a patterned substrate can occur if the plume is not perpendicular to the sample during deposition. As a matter of fact, the laser always points on the same region of the target creating a groove in the target. Such feature has been tackled by grinding the target before deposition and by rotating it during deposition. Increasing the thickness of the specimen layer with respect to the actuator layer is another way to ensure that the overlap is not the weakest link. However, in this study, all the tensile test structures of interest where located on a surface area of ~ 2 cm^2 which is by far more than the surface where the PLD ensures a homogeneous thickness. For that reason, control of the optimum thickness is hardly possible and specimens tested in this study exhibit thickness in between 150 and 300 nm. By design, thinner specimens are more prone to experience more deformation while there is more chance that the overlap will be the weakest link.

Even if 25 μm long specimens exhibit some degree of non-linearity, it is not obvious that a-olivine entered any sort of plasticity regime. The specimens clearly show some time dependent behavior which is responsible for a decrease in stress and an increase in strain. The first measurement on these test structures was performed one hour after the actuation as TOC is not an in situ experiment. Therefore, the initial equilibrium position of the test structures just after etching the silicon substrate is probably at a lower specimen strain closer to the assumed linear elastic behavior. Moreover, the data have been corrected to account for linear elasticity of the wider part of the dog-bone specimens and DIC performed on similar specimens suggests that the behavior at small strain might be a lot more complex that linear elasticity (see Fig. 8). Any plastic behavior in the wider part of the specimen implies an overestimation of the reported strain which also suggests that the macroscopic yield stress is probably higher than 1.5 GPa. Extraction of the uniaxial tensile behavior above that stress could only be performed via the TOC method with a design change (narrower specimen to avoid overlap cracking, longer actuators) or preferably using an in situ tensile test technique such as in [18,19],.

4.2. Time dependent response

The ability of the TOC method to perform relaxation tests has been demonstrated in earlier studies [12,20,21],. Here, the stability of the LPCVD Si_3N_4 as an actuator has been demonstrated as relaxation tests have been performed on freestanding a-olivine thin films for a timespan of more than 2 years without monopolizing any extra test equipment. Strain rates as low as 10^{-12} s^{-1} were investigated a value never explored before to the best of the author's knowledge.

The mean strain rate sensitivity parameter extracted on 13 different tensile tests is 0.054 which is very close to the 0.052 obtained by Baral et al. [8] by nanoindentation. Note that Baral et al. [8] were able to extract a stable value for the strain rate sensitivity parameter in the 10^{-4}–10^{-7} s^{-1} strain rate range. This single value for a-olivine thin films is thus extended for another 5 orders of magnitude (10^{-7} and 10^{-12} s^{-1}) in the present study.

Only one test structure (100 μm long specimen) gives a lower value of the strain rate sensitivity (0.033) (see Table 1 and Fig. 7). Unfortunately, this result cannot be confirmed as specimens with similar geometry could not be released properly due to local lithography problem during microfabrication. Further work will aim at confirming the value of the strain rate sensitivity for higher initial stress levels.

4.3. Linear elastic behavior of a-olivine

As highlighted before, all test structures experience stress relaxation independent of the stress level. The first measurement is not performed at time 0 which affects the apparent shape of the engineering stress-strain curve, including the slope of the linear part. In Section 3 as well as in Fig. 6b, the reported value of 107 GPa is considered as the most accurate measurement of Young's modulus of a-olivine because of the geometry of specimens which gives small errors on stress and strain extraction but also because these specimens experience relaxation at initial very low strain rate (10^{-9} s^{-1}). Consequently, the extraction of Young's modulus from the linear fit on the data from the first measurement is the least affected by relaxation.

The methodology to unload deformed specimens by cutting the actuator after release was used for the first time on TOC and should be

generalized for other materials deformed with this technique. It is indeed a straightforward way to extract accurate values of the Young's modulus value in the case of materials exhibiting similar relaxation rates. Indeed, the measurement is performed right after unloading as opposed to the one hour waiting time needed between actuation and measurement for the loading part in the usual procedure. The measured position after cutting was stable over time and gives values 10–20 % lower than the 107 GPa measured upon loading. This is partly due to the dog-bone shape of specimens as the displacement measurement is extracted out of the dog-bone region. In that regard, the 800 μm long rectangular specimen has again a more suitable geometry with no dog-bone affected zone and gives a value of 103 GPa, very close to the measurement upon loading. All in all, the value extracted on uniaxial tensile testing of freestanding a-olivine is quite close to the 89–92 GPa determined by Baral et al. [8] on an a-olivine thin film on substrate by nanoindentation.

4.4. Discussion from DIC analysis heterogeneous strain, beam effect

Spatial heterogeneity is inherent to amorphous materials. In metallic glasses, the link between spatial heterogeneity and mechanical properties, whether elastic [22] or plastic, has already been highlighted several times [23–27]. These studies generally agree in distinguishing the coexistence of more deformable zones (sometimes referred to as liquid-like) and less deformable zones (referred to in parallel as solid-like). In metallic glasses, these regions are often interpreted as loosely or densely-packed. In these studies, the spatial scales of heterogeneities reported are often dependent on the techniques used (e.g. dynamic force microscopy [23]; static force spectroscopy [24]; nano-indentation [25–27], which makes comparisons between studies difficult. Here, nano-DIC reveals local strain heterogeneity taking place in a-olivine at a spatial resolution rarely reached in SEM-DIC studies – i.e. down to some 50 nm clusters diameter. As pointed out in the method section, the size of the clusters estimated by nano-DIC is an upper bound of the material heterogeneity. We observe at this scale the formation of more compliant islands where deformation further proceeds, inside a matrix which is mostly elastic. In the supplementary, Fig. S3 confirms this morphology is not an artefact from the DIC methodology. This cluster type morphology of the localized zone is not consistent with the occurrence of in plane 45° shear band nor of 45° shear band in the thickness nor with multiple normal necking-type localization. The localization mostly operates in a direction nearly perpendicular to the tensile axis. Fig. 9 shows the temporal evolution of these heterogeneities. The distribution curve evolves as follows during deformation it decreases in height, increases in width and shifts towards increasing strains. Heterogeneities are thus amplified, with the particular feature that local strains can be far larger than the nominal strain. For instance, at 1058 h, the distribution extends to 6 %, whereas the nominal strain is only 2.4 %. This composite material behavior probably represents the heterogeneities of the potential energy landscape of glass and results in certain characteristics of the mechanical properties. In particular, these heterogeneities may explain the occurrence of mechanical relaxation at any stress, i.e. the viscoelastic behavior. Even in the supposed elastic regime, local material clusters may experience local flow i.e. some microplasticity, and will therefore relax and expand with time.

Although we have no data on this subject at this stage, it is likely that the activation of deformation zones is stress-dependent. It is therefore understandable that a certain dispersion is observed in the measured elastic moduli. The same applies to strain-rate sensitivity. Although m values reported in Table 1 are globally consistent, there is a tendency for m to decrease with increasing applied stress. Such a correlation between strain-rate sensitivity and heterogeneities has already been found in metallic glasses by Gu et al. [28].

A-olivine's mechanical response is sensitive to the electron beam. Even at very low voltage (2 kV in this study), a strong interaction between the electron beam and the material leads to mechanical softening. Nevertheless, the softening effect induced by the electron beam is homogeneous in the scanned region. Therefore, the nano-DIC heterogeneities should not be affected. As the local deformation mechanism is accelerated by the presence of the electron beam, no direct comparison between the local strain state and the global relaxation response of the specimen can be performed.

It is also worth noting that, the early activation of relaxation together with the heterogeneities shown in Fig. 8 presents some similarities with the mechanisms invoked in the literature to explain the origin of the so-called 'secondary β-relaxation', considered as the principal source of dynamics in glasses [29–31]. It was reported that β-relaxation is activated in metallic glasses under stress or annealing (at relativity low T below T_g) and is expected to play an important role in dictating the structural relaxation [32] and deformation of metallic glasses [33,34],. Theoretical models suggest that β-relaxation in mechanically rigid glasses, especially in metallic glasses, should be processed by the translational motion of atoms localized in loosely packed regions [35]. This scheme certainly assumes that β-relaxation intrinsically correlates with the presence of structural heterogeneities in metallic glasses. Zhu et al., recently demonstrated an intrinsic correlation between β-relaxation and spatial heterogeneity in metallic glasses using amplitude-modulation dynamic atomic force microscopy (AM-AFM) [36].

β-relaxation could also take place during plastic deformation of metallic glasses [29]. In this case, the loosely packed regions are fertile sites for the activation of shear transformation zones (STZs). The denser clusters act as strong inclusions that retard catastrophic shear banding by hindering the percolation of STZs. Other studies showed that metallic nanoglasses with promoted β-relaxation exhibit enhanced microscale tensile plasticity [29,34,37,38],. However, despite intense efforts in the literature, there is still no direct experimental evidences on the elementary mechanisms controlling β-relaxation and the link with the mechanical response. Furthermore, deep investigation of β-relaxation in other families of glasses other than metallic glasses (such as silicates) can be hardly found in the literature. In the present work, as evidenced by the intensity line profile of Fig. S4, some heterogeneities can be found in the chemical composition where, for instance, a drop of Fe-Kα signal coincides with an increase of Mg-Kα. These heterogeneities occur at a scale of a few tenth of nanometers which is line with the upper bound size of 100 nm evidenced in the DIC maps of Fig. 8. The origin of the heterogeneity in the DIC map could also be linked to local fluctuations of atomic density and/or atomic order and different co-exiting metastable glassy phases generated by the high quench rate used in the PLD process. β-relaxation could thus be activated at the early stage of deformation and room temperature at weak sites (aided by the electron beam) leading to the heterogonous strain map of Fig. 8. More efforts are currently made to investigate the nature of these heterogeneities using advanced TEM. This could shed new light on the atomic-scale mechanisms involved in this phenomenon. Interpreting such behavior, could lead to precious information regarding the fine glass dynamic.

5. Conclusion

The intrinsic mechanical properties and the elementary deformation mechanisms of amorphous olivine thin films were investigated using tensile-on-chip and DIC. The results can be summarized as follows

- Relaxation starts at the very early stage of deformation ($\varepsilon = 0.01\%$). This could be explained by the PLD process which probably leads to particularly high-energy out-of-equilibrium microstructures as opposed to a more relaxed glassy phase.
- Very low strain rate 10^{-12} s^{-1} was reached for the first time providing precious information on the rate dependent behavior of this material at time scales relevant for geodynamics.
- High strain rate sensitivity of 0.054 is measured together with the development of nanoscale strain heterogeneities revealed by DIC.

This is, again, in agreement with out-of-equilibrium microstructures involving local fluctuations of atomic density or atomic order.

- Differences between the local strain measured by DIC and the macroscopic strain provided by the TOC structures is observed. It can be attributed to the electron beam that might provide extra driving force for relaxation.
- The presence of strain heterogeneities together with the easy activation of relaxation at very low strain levels presents some similarities with β-relaxation. Further experiments are needed in order to investigate such feature in a-olivine.
- By giving access to relaxation tests at extremely low strain rates, the TOC method could play an important role for the investigation of the glass dynamics.

Declaration of competing interest

The authors declare that they have no known competing financial interests or personal relationships that could have appeared to influence the work reported in this paper.

Acknowledgements

This project has received funding from the European Research Council (ERC) under the European Union's Horizon 2020 research and innovation program under grant agreement No 787198 – TimeMan. H. Idrissi is mandated by the Belgian National Fund for Scientific Research (FSR- FNRS). This work was supported by the FNRS under Grant PDR – T011322F. The authors acknowledge the financial support from the 2020 Marcel de Merre prize awarded by the Fondation Louvain to P. Baral.

Supplementary materials

Supplementary material associated with this article can be found, in the online version, at doi:10.1016/j.actamat.2024.119693.

References

[1] V. Samae, P. Cordier, S. Demouchy, C. Bollinger, J. Gasc, S. Koizumi, A. Mussi, D. Schryvers, H. Idrissi, Stress-induced amorphization triggers deformation in the lithospheric mantle, Nature 591 (2021) 82–86, https://doi.org/10.1038/s41586-021-03238-3.

[2] H. Idrissi, A. Béché, N. Gauquelin, I. Ul-Haq, C. Bollinger, S. Demouchy, J. Verbeeck, T. Pardoen, D. Schryvers, P. Cordier, On the formation mechanisms of intragranular shear bands in olivine by stress-induced amorphization, Acta Mat 239 (2022) 118247, https://doi.org/10.1016/j.actamat.2022.118247.

[3] H. Idrissi, P. Carrez, P. Cordier, On amorphization as a deformation mechanism under high stresses, Curr. Opin. Solid State Mater. Sci. 26 (1) (2022) 100976, https://doi.org/10.1016/j.cossms.2021.100976.

[4] R. Jeanloz, T.J. Ahrens, J.S. Lally, G.L. Nord, J.M. Christie, A.H. Heuer, Shock-produced olivine glass first observation, Science 197 (1977) 457–459, https://doi.org/10.1126/science.197.4302.457.

[5] F. Guyot, B. Reynard, Pressure-induced structural modifications and amorphization in olivine compounds, Chem. Geol. 96 (1992) 411–420, https://doi.org/10.1016/0009-2541(92)90069-H.

[6] M. Blander, H.N. Planner, K. Kiel, L.S. Nelson, N.L. Richardson, The origin of chondrules experimental investigation of metastable liquids in the system Mg_2Si0_4-SiO_2, Geochim. Cosmochim. Acta 40 (1976) 889–892, https://doi.org/10.1016/0016-7037(76)90137-X.

[7] R. Dohmen, H.W. Becker, E. Meißner, T. Etzel, S. Chakraborty, Production of silicate thin films using pulsed laser deposition (PLD) and applications to studies in mineral kinetics, Eur. J. Mineral. 14 (2002) 1155–1168, https://doi.org/10.1127/0935-1221/2002/0014-1155.

[8] P. Baral, A. Orekhov, R. Dohmen, M. Coulombier, J.P. Raskin, P. Cordier, H. Idrissi, T. Pardoen, Rheology of amorphous olivine thin films characterized by nanoindentation, Acta Mat 219 (2021) 117257, https://doi.org/10.1016/j.actamat.2021.117257.

[9] C.Le Guillou, R. Dohmen, D. Rogalla, T. Müller, C. Vollmer, H.W. Becker, New experimental approach to study aqueous alteration of amorphous silicates at low reaction rates, Chem. Geol. 412 (2015) 179–192, https://doi.org/10.1016/j.chemgeo.2015.06.027.

[10] S. Gravier, M. Coulombier, A. Safi, N. André, A. Boé, J.P. Raskin, T. Pardoen, New on-chip nanomechanical testing laboratory - Applications to aluminum and polysilicon thin films, J. Microelectromech. Syst. 18 (2009) 555–569, https://doi.org/10.1109/JMEMS.2009.2020380.

[11] S. Jaddi, M. Coulombier, J.P. Raskin, T. Pardoen, Crack on a chip test method for thin freestanding films, J. Mech. Phys. Solids 123 (2019) 267–291, https://doi.org/10.1016/j.jmps.2018.10.005.

[12] M. Coulombier, G. Guisbiers, M.S. Colla, R. Vayrette, J.P. Raskin, T. Pardoen, On-chip stress relaxation testing method for freestanding thin film materials, Rev. Sci. Instr. 83 (2012) 105004, https://doi.org/10.1063/1.4758288.

[13] N. Klavzer, S. Gayot, M. Coulombier, B. Nysten, T. Pardoen, Nanoscale digital image correlation at elementary fibre/matrix level in polymer–based composites, Composites Part A Appl. Sci. Manufact. 168 (2023) 107455, https://doi.org/10.1016/j.compositesa.2023.107455.

[14] J. Blaber, B. Adair, A. Antoniou, Ncorr open-Source 2D Digital Image Correlation Matlab Software, Exp. Mech. 55 (2015) 1105–1122, https://doi.org/10.1007/s11340-015-0009-1.

[15] A. Favache, S. Ryelandt, M. Melchior, G. Zeb, P. Carbonnelle, J.P. Raskin, J.P. T. Pardoen, A generic "micro-Stoney" method for the measurement of internal stress and elastic modulus of ultrathin films, Rev. Sci. Instrum. 87 (2016) 015002, https://doi.org/10.1063/1.4939912.

[16] A. Boé, A. Safi, M. Coulombier, T. Pardoen, J.P. Raskin, Internal stress relaxation based method for elastic stiffness characterization of very thin films, Thin Solid Films 518 (2009) 260–264, https://doi.org/10.1016/j.tsf.2009.06.062.

[17] A. Velazco, A. Béché, D. Jannis, J. Verbeeck, Reducing electron beam damage through alternative STEM scanning strategies, Part I experimental findings, Ultramicroscopy 232 (2022) 113398, https://doi.org/10.1016/j.ultramic.2021.113398.

[18] V. Samae, R. Gatti, B. Devincre, T. Pardoen, D. Schryvers, H. Idrissi, Dislocation driven nanosample plasticity new insights from quantitative in-situ TEM tensile testing, Sci Rep. 8 (2018) 12012, https://doi.org/10.1038/s41598-018-30639-8.

[19] M. Ghidelli, A. Orekhov, A.Li Bassi, G. Terraneo, P. Djemia, G. Abadias, M. Nord, A. Béché, N. Gauquelin, J. Verbeeck, J.P. Raskin, D. Schryvers, T. Pardoen, H. Idrissi, Novel class of nanostructured metallic glass films with superior and tunable mechanical properties, Acta Mat 213 (2021) 116955, https://doi.org/10.1016/j.actamat.2021.116955.

[20] M.S. Colla, B. Amin-Ahmadi, H. Idrissi, L. Malet, S. Godet, J.P. Raskin, D. Schryvers, T. Pardoen, Dislocation-mediated relaxation in nanograined columnar palladium films revealed by on-chip time-resolved HRTEM testing, Nature Comm 65 (2015) 5922, https://doi.org/10.1038/ncomms6922.

[21] H. Idrissi, M. Ghidelli, A. Béché, S. Turner, S. Gravier, J.J. Blandain, J.P. Raskin, D. Schryvers, T. Pardoen, Atomic-scale viscoplasticity mechanisms revealed in high ductility metallic glass films, Sci. Rep. 9 (2019) 13426, https://doi.org/10.1038/s41598-019-49910-7.

[22] B.A. Sun, Y.C. Hu, D.P. Wang, Z.G. Zhu, P. Wen, W.H. Wang, C.T. Liu, Correlation between local elastic heterogeneities and overall elastic properties in metallic glasses, Acta Mater. 121 (2016) 266–276, https://doi.org/10.1016/j.actamat.2016.09.014.

[23] Y.H. Liu, D. Wang, K. Nakajima, W. Zhang, A. Hirata, T. Nishi, A. Inoue, M. W. Chen, Characterization of nanoscale mechanical heterogeneity in a metallic glass by dynamic force microscopy, Phys. Rev. Lett. 106 (2011) 125504, https://doi.org/10.1103/PhysRevLett.106.125504.

[24] M. Gao, J.H. Perepezko, Mapping the viscoelastic heterogeneity at the nanoscale in metallic glasses by static force spectroscopy, Nano Lett. 20 (2020) 7558–7565, https://doi.org/10.1021/acs.nanolett.0c03026.

[25] W.W. Qiu, Y. Ma, Revealing the length-scale dependence of the spatial mechanical heterogeneity and shear transformation zone size in metallic glassy films, Thin Solid Films 768 (2023) 139733, https://doi.org/10.1016/j.tsf.2023.139733.

[26] B. Riechers, C. Ott, S.M Das, C.H. Liebscher, K. Samwer, P.M. Derlet, R. Maaß, On the elastic microstructure of bulk metallic glasses, Mater Des 229 (2023) 111929, https://doi.org/10.1016/j.matdes.2023.111929.

[27] P. Tsai, K. Kranjc, K.M. Flores, Hierarchical heterogeneity and an elastic microstructure observed in a metallic glass alloy, Acta Mater. 139 (2017) 11–20, https://doi.org/10.1016/j.actamat.2017.07.061.

[28] Y. Gu, X. Han, F. Yan, L. Li, The strain rate sensitivity of heterogeneous thin film metallic glasses interplay between nanoscale heterogeneity and dynamic plasticity, Front. Mater. 9 (2022) 925096, https://doi.org/10.3389/fmats.2022.925096.

[29] W.H. Wang, Dynamic relaxations and relaxation property relationships in metallic glasses, Prog. Mater. Sci. 106 (2019) 100561, https://doi.org/10.1016/j.pmatsci.2019.03.006.

[30] K.L. Ngai, S. Capaccioli, M. Paluch, L. Wang, Clarifying the nature of the Johari-Goldstein beta-relaxation and emphasising its fundamental importance, Philos. Mag. 100 (2020) 2596–2613, https://doi.org/10.1080/14786435.2020.1781276.

[31] Y. Sun, S.X. Peng, Q. Yang, F. Zhang, M.H. Yang, C.Z. Wang, K.M. Ho, H.B. Yu, Predicting complex relaxation processes in metallic glass, Phys. Rev. Lett. 123 (2019) 105701, https://doi.org/10.1103/PhysRevLett.123.105701.

[32] L.N. Hu, Y.Z. Yue, Secondary relaxation in metallic glass formers its correlation with the genuine Johari-Goldstein relaxation, J. Phys. Chem. C 113 (2009) 15001–15006, https://doi.org/10.1021/jp903777f.

[33] W.H. Wang, Correlation between relaxations and plastic deformation, and elastic model of flow in metallic glasses and glass-forming liquids, J. Appl. Phys. 110 (2011) 053521, https://doi.org/10.1063/1.3632972.

[34] H.B. Yu, X. Shen, Z. Wang, L. Gu, W.H. Wang, H.Y. Bai, Tensile plasticity in metallic glasses with pronounced β relaxations, Phys. Rev. Lett. 108 (2012) 015504, https://doi.org/10.1103/PhysRevLett.108.015504.

[35] G.P. Johari, Localized molecular motions of beta-relaxation and its energy landscape, J. Non Cryst. Solids 307 (2002) 317–325, https://doi.org/10.1016/S0022-3093(02)01491-6.

[36] F. Zhu, H.K. Nguyen, X. Song, DP.B. Aji, A. Hirata, H. Wang, K. Nakajima M. W. Chen, Intrinsic correlation between β-relaxation and spatial heterogeneity in a metallic glass, Nature Commun. 7 (2016) 11516, https://doi.org/10.1038/ncomms11516.

[37] Z. Wang, W.H. Wang, Flow units as dynamic defects in metallic glassy materials, Natl. Sci. Rev. 6 (2019) 304, https://doi.org/10.1093/nsr/nwy084.

[38] Q. Wang, S. Zhang, Y. Yang, Y. Dong, C. Liu, J. Lu, Unusual fast secondary relaxation in metallic glass, Nat. Commun. 6 (2015) 7876, https://doi.org/10.1038/ncomms8876.